SCIENTIFIC REPORTS
nature research

Check for updates

OPEN

Flexible endoscopic micro-optical coherence tomography for three-dimensional imaging of the arterial microstructure

Junyoung Kim[1,6], Sunwon Kim[2,3,6], Joon Woo Song[3,6], Hyun Jung Kim[3], Min Woo Lee[4], Jeongmoo Han[5], Jin Won Kim[3,7] ✉ & Hongki Yoo[5,7] ✉

Micro-optical coherence tomography (μOCT) is a novel imaging approach enabling visualization of the microstructures of biological tissues at a cellular or sub-cellular level. However, it has been challenging to develop a miniaturized flexible endoscopic μOCT probe allowing helical luminal scanning. In this study, we built a flexible endoscopic μOCT probe with an outer diameter of 1.2 mm, which acquires three-dimensional images of the arterial microstructures via helical scanning with an axial and lateral resolutions of 1.83 μm and 3.38 μm in air, respectively. Furthermore, the depth of focus of the μOCT imaging probe was extended two-fold using a binary phase spatial filter. We demonstrated that the present endoscopic μOCT could image cellular level features of a rabbit artery with high-risk atheroma and a bioresorbable scaffold-implanted swine coronary artery. This highly-translatable endoscopic μOCT will be a useful tool for investigating coronary artery disease and stent biology.

Optical coherence tomography (OCT) is an optical imaging technique that provides tomographic images of biological samples[1]. Owing to its high spatial resolution, fast imaging speed, and high sensitivity, OCT is currently widely used in diagnosing diseases and guiding treatment strategies in various medical fields, such as ophthalmology, oncology, and cardiology[2–7]. In particular, intravascular OCT has become a mainstay imaging modality for coronary artery disease, offering high-resolution imaging of luminal microstructures such as atherosclerotic plaques, intraluminal thrombus, bifurcation anatomy, and coronary stents[8–11]. Although OCT provides highly detailed images (spatial resolution of 10 to 30 μm)[12–14], it is as yet insufficient for visualizing cellular- or subcellular-level structures, which may be essential for studying the progression and regression of the disease. To address this unmet need, researchers have striven to develop an advanced OCT imaging system with a higher resolution[15–17], i.e., a micro-OCT (μOCT) technique, which, albeit being a bulky benchtop platform, now allows a spatial resolution of up to 1 μm[18]. The enhanced spatial resolution of μOCT enabled visualization of cellular structures in various organs, such as the blood vessels, colon, and cornea[15,18,19].

To achieve cellular-level resolution, a broadband light source and high-numerical-aperture imaging lens must be used[20], however, the utilization of such apparatus leads to an increase in imaging probe diameter, limiting its broader clinical applications. Furthermore, the depth of focus (DOF) shortens in inverse proportion to the square of the lateral resolution gain and the DOF shortening means that the area of visualization is reduced. Our group has recently developed a miniaturized endoscopic μOCT system that provides images with an axial and lateral resolution of 2.49 μm and 2.59 μm, respectively[21,22]. Together with a small-diameter gradient-index (GRIN) lens, a binary phase spatial filter (BPSF) was incorporated into the system to overcome the trade-off between the resolution and DOF; consequently the DOF was extended two-fold. Although the system successfully visualized the arterial microstructure via linear scanning, its application as an intravascular imaging modality was still limited

[1]Mechanical Engineering Research Institute, KAIST, Daejeon, 34141, Republic of Korea. [2]Department of Cardiology, Korea University Ansan Hospital, Ansan, 15355, Republic of Korea. [3]Multimodal Imaging and Theragnostic Laboratory, Cardiovascular Center, Korea University Guro Hospital, Seoul, 08308, Republic of Korea. [4]Center for Robotics Research, Korea Institute of Science and Technology, Seoul, 02792, Republic of Korea. [5]Department of Mechanical Engineering, KAIST, Daejeon, 34141, Republic of Korea. [6]These authors contributed equally: Junyoung Kim, Sunwon Kim and Joon Woo Song. [7]These authors jointly supervised this work: Jin Won Kim and Hongki Yoo. ✉e-mail: kjwmm@korea.ac.kr; h.yoo@kaist.ac.kr

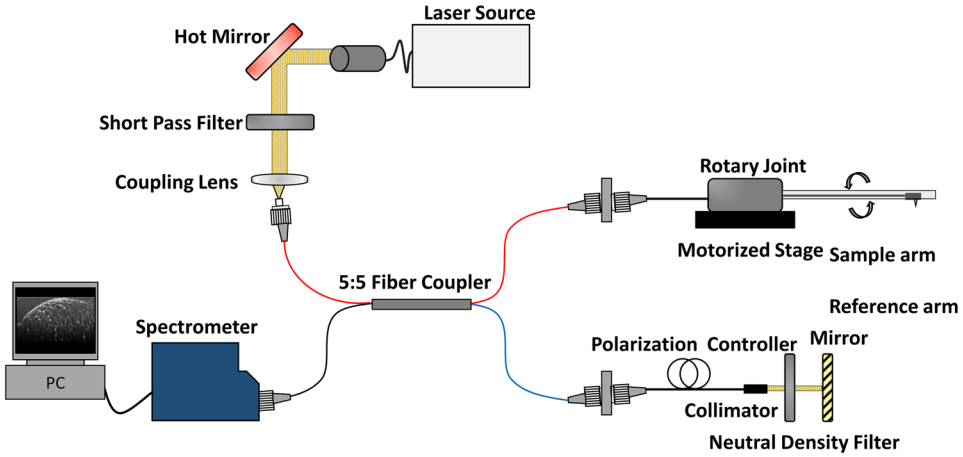

Figure 1. Schematic diagram of the developed endoscopic μOCT system for three-dimensional vascular imaging.

due to a lack of helical scanning capability. In this study, we report our experience with using a flexible low-profile endoscopic μOCT imaging probe and a dedicated optical rotary junction that allow full 360° helical scanning. This cutting-edge μOCT imaging modality provides high-resolution tomographic images with axial and lateral resolution of 1.83 μm and 3.38 μm, respectively, while maintaining the extended DOF. To demonstrate the feasibility of the present technique for intravascular imaging, we tested it using a healthy swine coronary artery, a bioresorbable vascular scaffold (BVS)-implanted swine coronary artery, and a rabbit artery with high-risk atherosclerotic plaques.

Results

Characterization of the endoscopic μOCT system. Figure 1 presents a schematic diagram of the endoscopic μOCT system. The system was built on the basis of a spectral-domain OCT using a supercontinuum laser (see the "Methods" section). The spectrometer determines the maximum a-line rate of the system at 40 kHz. The sensitivity of the system was 93.02 dB, which was measured using a mirror and neutral density filter. The scanning part was constructed using a laboratory-built rotary joint and motorized stage (see "Methods" section). A schematic diagram of the rotary joint developed for the three-dimensional vascular imaging is shown in Fig. 2a. The maximum rotational speed was 100 rps, and the measured throughput was 75.14% at center wavelength. The experimental transmission results depending on the rotational angle of the rotary joint are shown in Fig. 2b. The measured optical throughput variation upon rotation was within 6.2%. In addition, spectral measurements confirmed that all wavelengths in the ranges passed through the rotary joint, and there was no wavelength cut off as designed (Fig. 2c).

Figure 3a shows an imaging probe of the endoscopic μOCT system. The imaging probe was composed of 1 mm diameter optics and a binary phase spatial filter (BPSF) to increase the imaging range, which has a gain of 1.91. A photograph of the flexible imaging probe wrapped in a steel tube to protect it from impact and contamination is shown in Fig. 3b. The details of the fabrication methods are described in the "Methods" section. The length of the rigid portion of the imaging probe was 6.6 mm, and the outer diameter of the steel tube was 1.2 mm. Our flexible imaging catheter could provide images without non-uniform rotational distortion while the catheter shaft was being bent significantly (see Supplementary Materials and Fig. S1). The point spread function (PSF) of the imaging probe is shown in Fig. 3c. Figure 3d shows a representative cross-sectional profile of the transverse PSF. The lateral resolution, defined as full-width at half maximum (FWHM) of the intensity distribution, is 3.38 μm in the air. A normalized axial profile of a reflecting surface, shown in Fig. 3e, had a 1.83 μm axial resolution as calculated from the FWHM of the axial profile in the air.

μOCT imaging of a healthy swine coronary artery. A freshly resected healthy swine coronary was imaged using a custom-made imaging chamber filled with phosphate-buffered saline (Supplementary Fig. S2). The fluorinated ethylene propylene-tubed μOCT imaging probe with an outer diameter of 1.65 mm was safely inserted into the artery. Figure 4a shows the representative cross-sectional image acquired using μOCT. Owing to the improved spatial resolution and increased DOF, the structure of the muscular arterial wall was well visualized as clearly distinguishable three layers, namely, tunica intima, tunica media and tunica adventitia (Fig. 4a). Furthermore, unlike conventional OCT showing the tunica media as a single ill-defined low-scattering layer, our μOCT technique fully characterized the laminated architecture of the medial layer consisting of multiple smooth muscle cell (SMC) sheets intermixed with elastic fiber (bright lines, Fig. 4a–c).

The internal elastic lamina (IEL) is a very thin elastic fiber layer separating the intima and media (Fig. 4b, white arrows) that is not readily identifiable with conventional OCT (Fig. 4d). In the process of atherosclerosis, the IEL serves as a restrictive barrier to molecular movement into the intima[23]. An injured IEL during angioplasty or stenting provides a gateway for immune cells and SMCs, consequently leading to excessive neointimal proliferation, i.e. restenosis. Furthermore, disruption or loss of the IEL contributes to the development of various

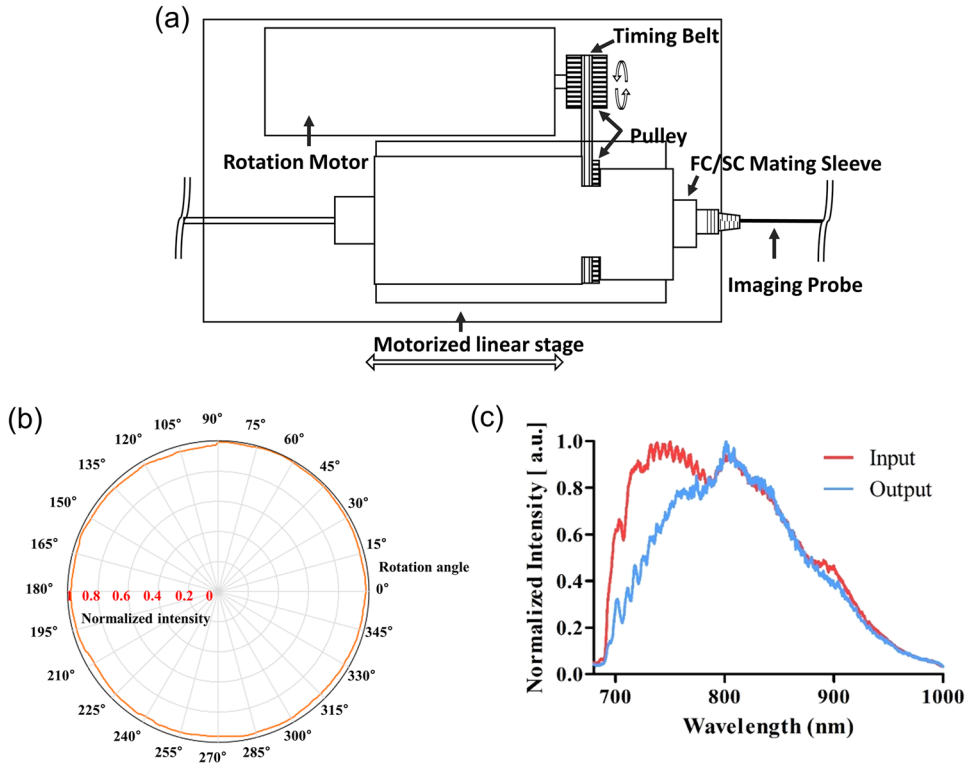

Figure 2. (**a**) Schematic diagram of the developed rotary joint and pullback stage for three-dimensional vascular imaging; (**b**) Experimental results of the normalized optical power throughput depending on the rotational angle of the rotary joint; (**c**) Experimental results of the spectral throughput of the rotary joint over the entire wavelength of the designed light source.

vasculopathies such as coronary ectasia, aneurysm, and fibromuscular dysplasia[24,25]. With the present μOCT system, the IEL was clearly visualized as a highly scattering linear structure near the luminal surface (Fig. 4b, white arrows). A high index of refraction of elastin and its fibrous structure is thought to act as a robust scatterer of light[26]. We also detected fragmentation of the IEL (Fig. 4b, red arrowheads) at the coronary bifurcation, a preferred site for atherosclerosis where the endothelium is exposed to altered shear stress[27]. Previous experimental studies using surgically created bifurcation animal models reported a similar observation, i.e. IEL damage occurred at the periapical region of the bifurcation which experienced high shear stress[28,29].

μOCT imaging of coronary bioresorbable vascular scaffold (BVS) healing. Coronary arterial healing following stent implantation is a natural reparative process involving a cascade of endothelial denudation, peri-strut blood clot formation, inflammatory reaction, and finally strut-coverage by newly formed intimal tissue, i.e. neointima[30]. Figure 5 shows the findings from a swine coronary artery with a BVS implanted 7 days ago. It is well known that stent-related arterial inflammation is mainly driven and regulated by macrophages[30,31]. After a neutrophil-mediated brisk early inflammatory response, monocytes infiltrate into the platelet-rich mural thrombus, forming aggregated macrophages clusters around struts[31]. As clearly shown in Fig. 5, the infiltrated macrophages, appeared as distinct bright spots in the μOCT (Fig. 5a and a), were present around the BVS struts. However, in conventional OCT, the BVS struts were surrounded by thick tissue with a relatively homogenous signal intensity (Fig. 5b and b). Peri-strut macrophage infiltration was verified in the corresponding histologic section stained with PM-2K anti-macrophage antibody (Fig. 5c).

After intravascular stent implantation, the protruded strut disrupts the coronary laminar flow, creating a flow stagnation zone around the struts, which triggers platelet aggregation and fibrin deposition[32]. Fibrin, if deposited at a physiological level, is internalized and degraded by macrophages[30]. However, excessive fibrin deposition, typically observed as a peri-strut low intensity area on OCT, is a marker of maladaptive stent healing and a precursor of stent-related complication[33,34]. Also, experimental and clinical studies have clearly shown that the overlapping stent segments harbor more fibrin and inflammatory cell deposition than the non-overlapping sites[35], and were associated with worse clinical outcomes[36]. Figure 6 presents a μOCT image obtained in an arterial segment stented with two overlapping BVSs. The entire μOCT imaging data is provided in Supplementary Movie 1. Using our μOCT technique, the peri-strut fibrin deposition (Fig. 6a,a and c) was more clearly visualized compared to that with conventional OCT (Fig. 6b and b). Moreover, even physiologic-level fibrin deposition could be observable with our μOCT imaging (Supplementary Fig. S3). The current imaging based on helical luminal scanning could readily provide a three-dimensional image of arterial structure of interest, facilitating an intuitive and comprehensive interpretation (Fig. 6d).

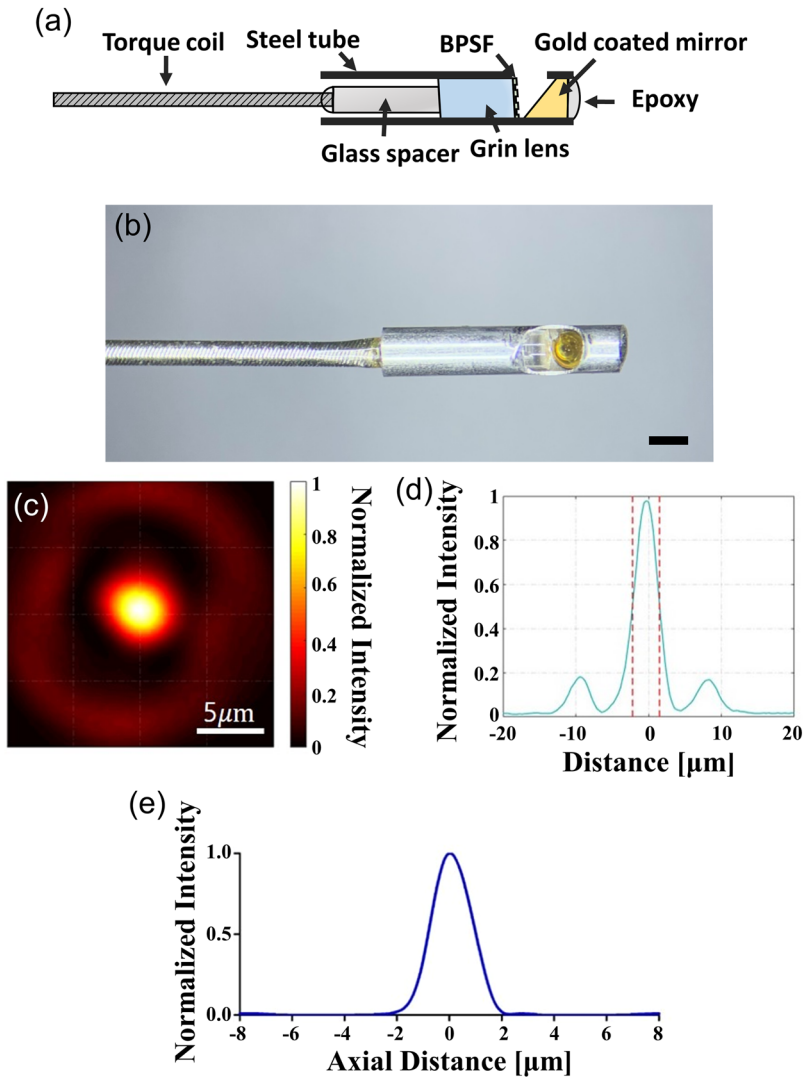

Figure 3. (**a**) Schematic diagram and (**b**) Photograph of the developed imaging probe. Scale bar, 1 mm; (**c**) Two-dimensional transverse PSF of the focused imaging system; (**d**) Cross-sectional profile of the PSF; (**e**) Normalized axial profile of a reflecting surface.

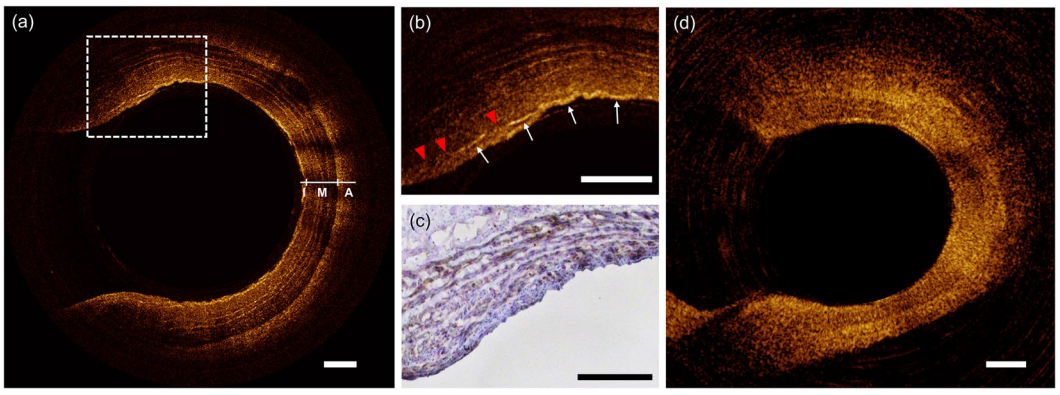

Figure 4. (**a**) μOCT image of a healthy swine coronary artery shows trilaminar vessel architecture of a muscular artery. I = intima; M = media; A = adventitia. (**b**) High magnification image at the bifurcation demonstrating partial loss (red arrowheads) of IEL (white arrows); (**c**) Corresponding immunohistological staining image for smooth muscle cells (α-SMA stain); (**d**) Image acquired using conventional OCT. Scale bars, 200 μm.

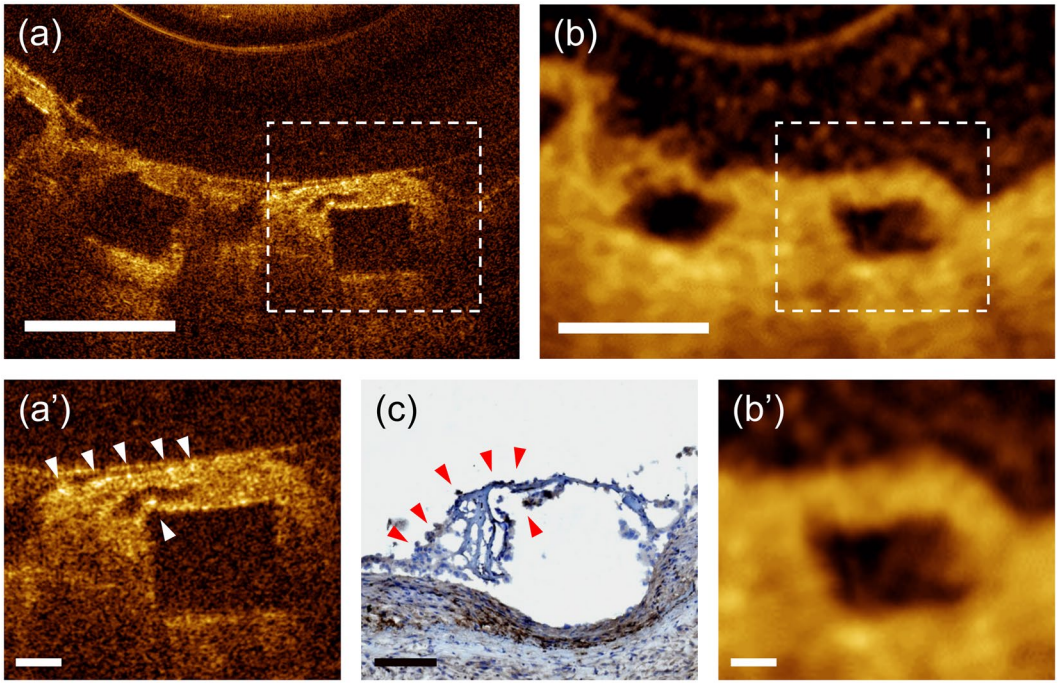

Figure 5. (**a**) Cross-sectional μOCT image of the swine coronary artery with a BVS implanted 7 days prior to imaging; (**b**) Corresponding conventional OCT image; (**a'**) A magnified μOCT image shows the infiltrated macrophages (bright spots, white arrowheads) around struts; (**b'**) Conventional OCT show neointimal tissue with relatively uniform signal intensity; (**c**) Corresponding anti-macrophage immunostaining findings corroborate the μOCT imaging findings (red arrowheads). Scale bars for **a** and **b**, 500 μm. Scale bars for **a'** and **b'**, 100 μm.

The capability of μOCT to characterize the IEL was still effective in case of BVS-implanted artery covered with mature neointima (28 days post-implantation). Altered IEL geometry due to vascular scaffolding was clearly delineated with our μOCT (Fig. 7a and a'), while conventional OCT visualized a vague line connecting the contiguous struts (Fig. 7b and b') in a limited area only. Fully expanded BVS struts compressed and stretched the IEL outward into the medial layer (Fig. 7a and c). The finding of correlative Verhoeff elastic-Masson trichrome (VMT) staining, which allows differentiation of elastin (black), corroborated accurately with the μOCT imaging findings (Fig. 7a and c) Neointimal thickness after stenting is an efficacy measure of individual stent and is currently calculated by drawing an arbitrary circular line interconnecting the stent struts[5]. However, as demonstrated in Fig. 7, the IEL geometry after stenting was not complete circular in shape and could be altered further in diseased arteries. Furthermore, coronary stenting inevitably causes hyperstretch vessel injury and resultant IEL rupture induces excessive neointimal proliferation, consequently leading to stent failure[37]. Such arterial response to severe vessel injury was still substantial despite the use of newer stents coated with antiproliferative drug[38]. The present higher-resolution approach is expected to provide better imaging guidance to optimize the stent implantation and to monitor the stent efficacy.

μOCT imaging for detecting microcalcification in atherosclerotic plaques. To investigate whether the current μOCT system can identify the microstructural feature that leads to atherosclerotic plaque destabilization, a rabbit model of atherosclerotic calcification was developed and imaged. In the cross-sections with bunch plaque formation, conventional OCT showed a poorly-delineated signal-poor lesion implying a high-risk plaque (Fig. 8a). Some punctate signal-rich structures near the luminal surface, albeit not clearly discernible, suggested the macrophages infiltration (Fig. 8a'). However, unlike the findings from conventional OCT, the abluminal area contained a multiple punctate or confluent bright spots with signal attenuation in μOCT (Fig. 8b and b'). To determine the origin of the spotty bright signals in μOCT image, we performed histologic validation using von Kossa staining for evaluating calcification (Fig. 8c and c'); haematoxylin-eosin (H&E) staining for morphological characteristics (Fig. 8d and d'); and RAM11 immunohistochemical staining for macrophage infiltration (Fig. 8e and e'). Histopathologic evaluation of the corresponding histologic section revealed that the lesion was macrophage-abundant plaque with microcalcification (Fig. 8c'–e'). The bright spots in the μOCT scans corresponded with the calcium-positive areas (black) in the von Kossa-stained histologic section (Fig. 8b' and ç'), supporting that the current μOCT system could specifically detect the plaque microcalcification. Conversely, bright spots were not noted in the plaques without surface microcalcification (Fig. 8g-j).

Intimal microcalcification, i.e. calcium deposits approximately 5–60 μm in diameter, is currently considered a marker of plaque vulnerability because microcalcification amplifies the local stress on the fibrous cap and increase the risk of plaque rupture[39–41]. 18F-NaF positron emission tomography-computed tomography is currently the only imaging modality that can detect atherosclerotic microcalcification;[41] however, its application in coronary

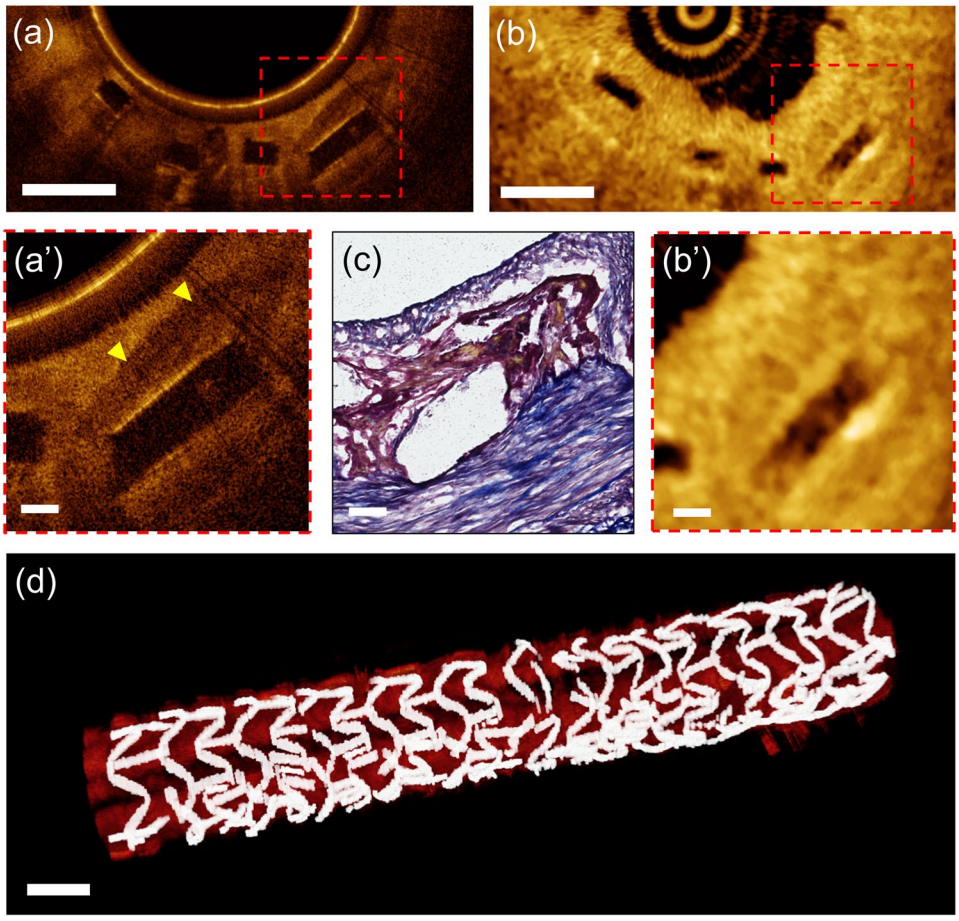

Figure 6. Imaging results of a swine coronary artery that received two overlapping BVSs (28 days post-implantation). (**a,a'**) μOCT image clearly demonstrating a peri-strut low-intensity area with well-defined margin (yellow arrowheads); (**b,b'**) Corresponding cross-section acquired using conventional OCT; (**c**) Histologic section shows excessive fibrin deposition around strut (Verhoeff elastic-Masson trichrome stain). (**d**) A three-dimensionally reconstructed image of BVSs-implanted swine coronary artery (28 days post-implantation) showing multiple fractured struts. Three-dimensional volume rendering was performed using OsiriX (The OsiriX Foundation, Geneva, Switzerland). Scale bars for **a**, **b**, and **d** 500 μm. Scale bars for **a', b,'** and **c** 100 μm.

beds is limited due to its poor spatial resolution and presence of cardiac motion artifacts. In the present μOCT study, plaque microcalcification was visualized as distinct bright spot. OCT bright spot was conventionally considered to represent macropahges[42], however, a recent human autopsy study showed that bright spots can be generated by other plaque components that cause sharp changes in index of refraction[43]. In this reports, the interfaces between calcium and fibrous tissue, or between calcium and lipid were responsible for 15% of bright spot-positive regions[43]. We thought that the presence of dense calcium within macrophage-filled tissue led to a drastic change in refractive indices; thus yielded bright signals in μOCT image. The limited spatial resolution of conventional OCT may not be adequate for imaging this minute change that arise at the interface of tiny calcium.

Discussion

The introduction of intravascular OCT, an optical imaging technique providing 10-fold higher resolution than intravascular ultrasound, has further increased our understanding of coronary atherosclerosis during the last decade. In the present study, we demonstrated the feasibility of a flexible endoscopic μOCT system for intravascular imaging by testing it in coronary-sized vessels of various animal models, including a healthy swine coronary artery, BVS-implanted swine coronary artery, and rabbit artery with high-risk atherosclerotic plaques. Compared with the conventional OCT, the present technique could provide additional, cellular- or subcellular-level information relevant to atherogenesis, plaque destabilization, stent-artery interaction, and neointimal healing.

To build a clinically translatable intravascular μOCT imaging system, fabrication of miniaturized imaging probe with a helical scanning capability is warranted. It was previously reported that an endoscopic μOCT system was feasible for imaging the swine trachea *in vivo*[44], however, the rigid endoscope with an outer diameter of 4 mm limited its broader applications. Cui D *et al.* reported the fabrication of a flexible endobronchial μOCT probe with a diameter of 2.4 mm, incorporating a GRIN lens and an apodizing beam splitter to extend DOF[45]. However, tomographic imaging of the entire lumen could not be performed with this endoscopic μOCT system

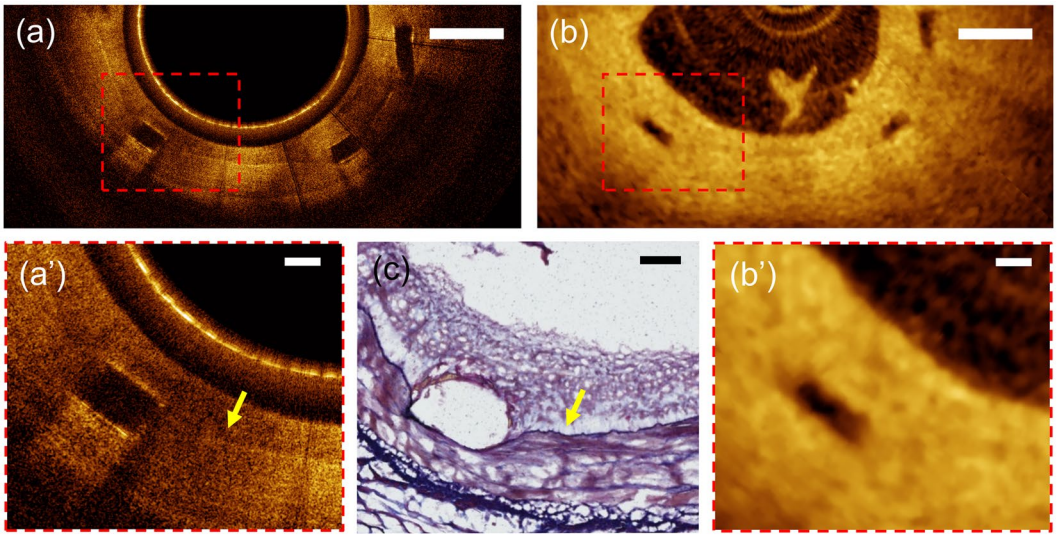

Figure 7. (**a**) μOCT image of a BVS-implanted swine coronary artery (28 days post-implantation) and (**b,b'**) corresponding cross-section of conventional OCT; (**a'**) A magnified μOCT image shows a thin highly-scattering IEL (arrow) that separates the medial layer and the strut-covering neointima; (**c**) Corresponding histologic section stained with Verhoeff elastic-Masson trichrome; Scale bars for a and b, 500 μm. Scale bars for a', b' and c, 100 μm.

that provided one-dimensional mapping only. Yuan W *et al*. developed an endoscopic μOCT imaging probe with a diameter of less than 1 mm and demonstrated its feasibility for visualizing the luminal organs of animal models[17]. Their imaging probe based on fiber-optic ball lens provided an axial resolution of 2.4 μm; but a sufficient level of transverse resolution (6 μm) was not achieved[17]. This mismatch may considerably hamper the detailed visualization of cellular or subcellular structures. More recently, Yin B *et al*. reported a μOCT system that innovatively extended DOF by implementing few-mode interferometry[46,47]. Their approach based on a small-diameter, flexible catheter successfully visualized cellular features of diseased human coronary arteries and coronary-sized arteries of living rabbits[46]. However, since each mode had a different NA, the lateral resolution created by each mode unavoidably varied, resulting in a non-uniform lateral resolution across depth (average lateral resolution of 3–4 μm)[46,47]. The present μOCT imaging system provided a cellular-level resolutions that were at least equivalent or superior to those reported previously. Moreover, our highly flexible, miniaturized imaging probe had a catheter profile equivalent to that of early intravascular ultrasound. We expect that this highly-translatable intravascular μOCT system allowing visualization of luminal microstructures at an unprecedented level of detail and sensitivity will provide a novel opportunity for the understanding of vascular biology and pathology.

Methods

Endoscopic μOCT system. The developed system is based on spectral-domain OCT. A supercontinuum laser (SC400-4, Fianium, Southampton, UK) was used as a light source, transmitting a center wavelength of 850 nm and a bandwidth to 280 nm through a hot mirror (M254H45, Thorlabs, Newton, NJ) and a short pass filter (FESH1000, Thorlabs). We confirmed that the light source was limited to the designed wavelength range using an optical spectrum analyzer. The light goes into an interferometer, which was constructed using a 5: 5 optical fiber coupler (TW850R5A2, Thorlabs) and polarization controller (FPC020, Thorlabs) through a coupling lens (AC050–008-B, Thorlabs). It was confirmed that the coupling efficiency was more than 70% at all wavelength bands used, through ZEMAX simulation. The scanning component was constructed using a lab-built rotary joint, motorized stage (A-LSQ075A, Zaber Technologies Inc., Vancouver, British Colombia, Canada) and the detection part was composed of a custom-designed spectrometer (2048 pixels, Wasatch Photonics, Morrisville, NC); the data were transferred to a computer. The signal obtained by the spectrometer was displayed in real-time as depth information and the processed image and saved on a computer. To acquire three-dimensional images, we developed a lab-built rotary joint for the μOCT system. The rotary joint consisted of two collimators that utilize the GRIN lens (SLW180023083X30, Go!Foton, Somerset, NJ), a rotating motor (3654K024B, Faulhaber, Schönaich, Germany), and a timing belt. One of the collimators was rotated for scanning through the timing belt which transmits the rotation force from the motor. The completed rotary joint was connected to the motorized pullback stage through a stage adapter for helical scanning of the imaging probe.

A schematic diagram of the imaging probe is shown in Fig. 3a. It was composed of a GRIN lens (X_W10-S0180–083-SOC X = 4DP, Go!Foton), glass spacer (FG550UEC, Thorlabs), single-mode fiber (750HP, Thorlabs) and gold-coated mirror. First, the single-mode fiber was fusion spliced to the glass spacer, and then precisely polished to a predefined length by polishing machine. The polished surface was angled at 4° to reduce noise caused by back-reflection. Second, the binary phase spatial filter (BPSF) applied GRIN lens and glass spacer were precisely monitored and aligned using a three-axis linear stage, and then bonded using UV curable epoxy. The BPSF pattern has annular patterns, and was fabricated using soft lithography techniques. The details of the

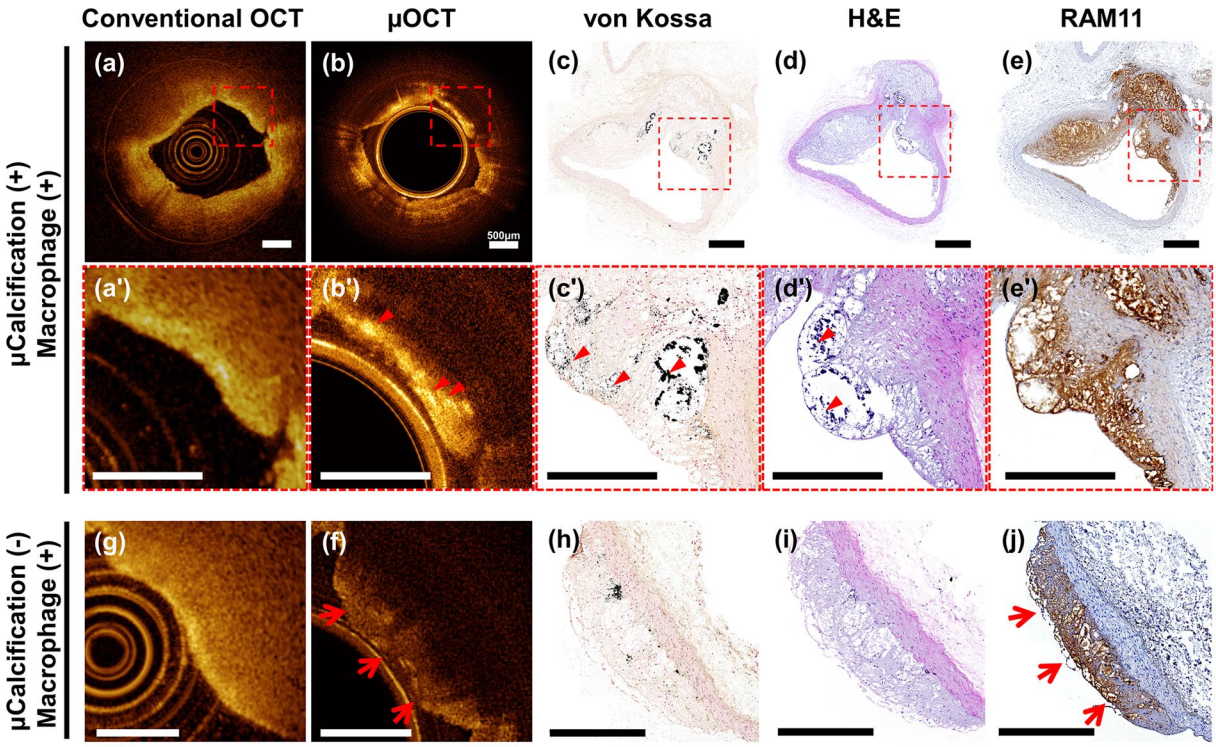

Figure 8. (**a – e'**) Comparison among conventional OCT, μOCT and histologic evaluation of a high-risk plaque with microcalcification; (**a,a'**) Conventional OCT images showing ill-defined signal-poor region; (**b,b'**) μOCT images showing multiple bright spots (red arrowheads); The red arrowheads indicate the corresponding microcalcification in μOCT (**b'**), von Kossa (**c'**) and H&E (**d'**), and RAM11 (**e'**) images; (**g–j**) Imaging findings from a plaque without surface microcalcification. Scale bars, 500 μm.

fabrication methods and performance of the BPSF are described in our previous publications[21,22]. Third, the imaging probe from the previous step was inserted in to a steel tube with an outer diameter of 1.21 mm, and the gold-coated mirror with an angle of 41° was inserted in the other side of the steel tube. The gold-coated mirror was aligned to allow light to propagate through the window of the steel tube. Thereafter, the entire fiber was encased in a torque coil (Asahi Intecc Co, Aichi, Japan) with outer/inner diameter of 0.65/0.27 mm for protection and transfer of torque for probe rotation and translation. 3D PSF of the imaging probe was measured using a 20x objective lens (#38–330, Edmund optics, Barrington, NJ) and a beam profiler (BC106N-VIS/M, Thorlabs). The objective lens and beam profiler were aligned using a three-axis linear translation stage. We analyzed the PFS at the focal plane defined as the axial position with the highest peak intensity of the measured PSF. The lateral resolution was defined as FWHM of the intensity distribution, which was determined by linear interpolation. When calculating lateral resolution, the side lobes were not considered due to their low intensity (81.8% lower than the main lobe). The axial profile was measured using a mirror (PF10–03-P01, Thorlabs) at the focal plane and axial resolution analyzed as FWHM of linearly interpolated data.

***Ex vivo* imaging protocol.** Imaging was performed twice in each blood vessel at a 10k A-line rate with a rotation speed of 120 rpm and a pullback speed of 50 μm/s and 500 μm/sec to achieve an interval between frames was 25 μm and 250 μm. Each blood vessel was also imaged using a conventional OCT system at the same position with the same frame interval (51.2k A-line rate with a rotation speed of 3000 rpm and pullback speed of 1.25 mm/s and 12.5 mm/s) to allow direct comparison against the μOCT. Intravascular OCT system, used in this study, was built based on a prototype device from a commercial OCT manufacturer (NinePoint Medical, Cambridge, MA, USA). The axial and lateral resolution, defined as FWHM of peak intensity at the focal plane, of the OCT system was 11.58 μm and 22.67 μm, respectively. Following imaging, the animal blood vessels were resected, fixed, and processed for histopathological analysis. All animal studies were approved by the Institutional Animal Care and Use Committee of Korea University College of Medicine (KOREA-2016-0170-C2 and KOREA-2018-0066), and all animal experiments procedures were performed in accordance with the relevant guidelines and regulations.

Swine model of BVS-implanted coronary artery. To investigate the early arterial healing process following intravascular stent implantation, a swine coronary stenting model was developed. Given that stent healing takes a month to complete in swine[48], we implanted BVSs twice, with a 3-week interval, and euthanized the animal at fourth week to investigate one BVS in the very early phase (7 days post-implantation) and the other in the final phase (28 days post-implantation) of stent healing simultaneously. The implanted BVSs were poly-L-lactic

acid-based polymeric stent (BRS, Suntech, Korea) with strut thickness of 100 μm and outer diameter of 2.5 mm. In the first procedure, we implanted two overlapping BVSs in the left anterior descending artery. *Ex vivo* imagings were performed using a custom-made imaging chamber (Supplementary Fig. S2), as previously described[49].

Rabbit model of atherosclerotic microcalcification. Rabbit model of atherosclerotic microcalcification was developed using previous methods with some modifications[50]. New Zealand white rabbits (male sex, 2.5–3.0 kg, DooYeol Biotech, Korea) were fed a high cholesterol diet containing vitamin K1 (1% cholesterol + 1.5 mg/g of vitamin K1; DooYeol Biotech) for 4 weeks and then with a high cholesterol-warfarin diet (1% cholesterol + 1.5 mg/g of vitamin K1 + 3 mg/g of warfarin; DooYeol Biotech), which was maintained for an additional 8 weeks.

Histologic validation. After μOCT imaging, the frozen swine coronary arteries were serially sectioned and stained. PM-2K monoclonal antibody (Abcam, Cambridge, UK) was used for the identification of plaque macrophages and α-SMA antibody (Abcam, Cambridge, UK) for SMCs. We used Modified VMT staining technique to highlight elastic fibers and other connective tissue elements. The rabbit arteries were fixed in 10% formalin and processed into paraffin-embedded blocks. Four-micrometer paraffin sections were prepared using a Leica RM2255 microtome (Leica Biosystems). The sections were deparaffinized and rehydrated, and then H&E and von Kossa (CVK-2-IFU, ScyTek Laboratories, West Logan, UT) staining were performed in accordance with the manufacturer's protocol. For immunohistochemical analysis, antigen retrieval was performed, endogenous peroxidase was blocked; and plaque macrophages were stained using RAM11 primary antibody (M0633, Agilent Dako, Santa Clara, CA). Tissue sections were then labelled with the Envision Polymer Detection System (Agilent Dako).

Received: 24 January 2020; Accepted: 6 May 2020;
Published online: 08 June 2020

References

1. Huang, D. *et al*. Optical coherence tomography. *Science* **254**, 1178–1181 (1991).
2. Wessels, R. *et al*. Optical biopsy of epithelial cancers by optical coherence tomography (OCT). *Lasers Med. Sci.* **29**, 1297–1305, https://doi.org/10.1007/s10103-013-1291-8 (2014).
3. Zysk, A. M., Nguyen, F. T., Oldenburg, A. L., Marks, D. L. & Boppart, S. A. Optical coherence tomography: a review of clinical development from bench to bedside. *J. Biomed. Opt.* **12**, 051403, https://doi.org/10.1117/1.2793736 (2007).
4. Fujimoto, J. G. Optical coherence tomography for ultrahigh resolution *in vivo* imaging. *Nat. Biotechnol.* **21**, 1361–1367, https://doi.org/10.1038/nbt892 (2003).
5. Tearney, G. J. *et al*. Consensus standards for acquisition, measurement, and reporting of intravascular optical coherence tomography studies: a report from the International Working Group for Intravascular Optical Coherence Tomography Standardization and Validation. *J. Am. Coll. Cardiol.* **59**, 1058–1072, https://doi.org/10.1016/j.jacc.2011.09.079 (2012).
6. Boppart, S. A., Luo, W., Marks, D. L. & Singletary, K. W. Optical coherence tomography: feasibility for basic research and image-guided surgery of breast cancer. *Breast Cancer Res. Treat.* **84**, 85–97, https://doi.org/10.1023/B:BREA.0000018401.13609.54 (2004).
7. Drexler, W. *et al*. Ultrahigh-resolution ophthalmic optical coherence tomography. *Nat. Med.* **7**, 502–507, https://doi.org/10.1038/86589 (2001).
8. Onuma, Y. *et al*. Joint consensus on the use of OCT in coronary bifurcation lesions by the European and Japanese bifurcation clubs. *Eurointervention* **14**, E1568–E1577, https://doi.org/10.4244/Eij-D-18-00391 (2019).
9. Raber, L. *et al*. Clinical use of intracoronary imaging. Part 1: guidance and optimization of coronary interventions. An expert consensus document of the European Association of Percutaneous Cardiovascular Interventions. *Eur. Heart J.* **39**, 3281–3300, https://doi.org/10.1093/eurheartj/ehy285 (2018).
10. Johnson, T. W. *et al*. Clinical use of intracoronary imaging. Part 2: acute coronary syndromes, ambiguous coronary angiography findings, and guiding interventional decision-making: an expert consensus document of the European Association of Percutaneous Cardiovascular Interventions. *Eur. Heart J.* **40**, 2566–2584, https://doi.org/10.1093/eurheartj/ehz332 (2019).
11. Kume, T. *et al*. Assessment of coronary arterial thrombus by optical coherence tomography. *Am. J. Cardiology* **97**, 1713–1717, https://doi.org/10.1016/j.amjcard.2006.01.031 (2006).
12. Jang, I. K. *et al*. Visualization of coronary atherosclerotic plaques in patients using optical coherence tomography: comparison with intravascular ultrasound. *J. Am. Coll. Cardiol.* **39**, 604–609 (2002).
13. Yun, S. H. *et al*. Comprehensive volumetric optical microscopy *in vivo*. *Nat. Med.* **12**, 1429–1433, https://doi.org/10.1038/nm1450 (2006).
14. Tearney, G. J. *et al*. Three-dimensional coronary artery microscopy by intracoronary optical frequency domain imaging. *JACC Cardiovasc. Imaging* **1**, 752–761, https://doi.org/10.1016/j.jcmg.2008.06.007 (2008).
15. Yuan, W. *et al*. Optimal operational conditions for supercontinuum-based ultrahigh-resolution endoscopic OCT imaging. *Opt. Lett.* **41**, 250–253, https://doi.org/10.1364/OL.41.000250 (2016).
16. Xi, J. *et al*. Diffractive catheter for ultrahigh-resolution spectral-domain volumetric OCT imaging. *Opt. Lett.* **39**, 2016–2019 (2014).
17. Yuan, W., Brown, R., Mitzner, W., Yarmus, L. & Li, X. Super-achromatic monolithic microprobe for ultrahigh-resolution endoscopic optical coherence tomography at 800 nm. *Nat. Commun.* **8**, 1531 (2017).
18. Liu, L. *et al*. Imaging the subcellular structure of human coronary atherosclerosis using micro-optical coherence tomography. *Nat. Med.* **17**, 1010–1014, https://doi.org/10.1038/nm.2409 (2011).
19. Ang, M. *et al*. Evaluation of a Micro-Optical Coherence Tomography for the Corneal Endothelium in an Animal Model. *Sci. Rep.* **6**, 29769, https://doi.org/10.1038/srep29769 (2016).
20. Popescu, D. P. *et al*. Optical coherence tomography: fundamental principles, instrumental designs and biomedical applications. *Biophys. Rev.* **3**, 155, https://doi.org/10.1007/s12551-011-0054-7 (2011).
21. Xing, J., Kim, J. & Yoo, H. Design and fabrication of an optical probe with a phase filter for extended depth of focus. *Opt. Express* **24**, 1037–1044, https://doi.org/10.1364/OE.24.001037 (2016).
22. Kim, J. *et al*. Endoscopic micro-optical coherence tomography with extended depth of focus using a binary phase spatial filter. *Opt. Lett.* **42**, 379–382, https://doi.org/10.1364/OL.42.000379 (2017).
23. Penn, M. S., Saidel, G. M. & Chisolm, G. M. Relative Significance of Endothelium and Internal Elastic Lamina in Regulating the Entry of Macromolecules into Arteries *in-Vivo*. *Circ. Res.* **74**, 74–82, https://doi.org/10.1161/01.Res.74.1.74 (1994).
24. Antoniadis, A. P., Chatzizisis, Y. S. & Giannoglou, G. D. Pathogenetic mechanisms of coronary ectasia. *Int. J. Cardiol.* **130**, 335–343, https://doi.org/10.1016/j.ijcard.2008.05.071 (2008).

25. Saw, J., Bezerra, H., Gornik, H. L., Machan, L. & Mancini, G. B. Angiographic and Intracoronary Manifestations of Coronary Fibromuscular Dysplasia. *Circulation* **133**, 1548–1559, https://doi.org/10.1161/CIRCULATIONAHA.115.020282 (2016).
26. Gouldstone, A., Caner, N., Swedish, T. B., Kalkhoran, S. M. & DiMarzio, C. A. Mechanical and optical dynamic model of lung. *IEEE Trans. Biomed. Eng.* **58**, 3012–3015, https://doi.org/10.1109/TBME.2011.2160346 (2011).
27. Davies, P. F. Hemodynamic shear stress and the endothelium in cardiovascular pathophysiology. *Nat. Clin. Pract. Cardiovasc. Med.* **6**, 16–26, https://doi.org/10.1038/ncpcardio1397 (2009).
28. Meng, H. *et al*. Complex hemodynamics at the apex of an arterial bifurcation induces vascular remodeling resembling cerebral aneurysm initiation. *Stroke* **38**, 1924–1931, https://doi.org/10.1161/Strokeaha.106.481234 (2007).
29. Kolega, J. *et al*. Cellular and Molecular Responses of the Basilar Terminus to Hemodynamics during Intracranial Aneurysm Initiation in a Rabbit Model. *J. Vasc. Res.* **48**, 429–442, https://doi.org/10.1159/000324840 (2011).
30. Chaabane, C., Otsuka, F., Virmani, R. & Bochaton-Piallat, M. L. Biological responses in stented arteries. *Cardiovasc. Res.* **99**, 353–363, https://doi.org/10.1093/cvr/cvt115 (2013).
31. Welt, F. G. & Rogers, C. Inflammation and restenosis in the stent era. *Arterioscler. Thromb. Vasc. Biol.* **22**, 1769–1776, https://doi.org/10.1161/01.atv.0000037100.44766.5b (2002).
32. Tenekecioglu, E. *et al*. The Effect of Strut Protrusion on Shear Stress Distribution Hemodynamic Insights From a Prospective Clinical. *Trial. Jacc-Cardiovasc Inte* **10**, 1803–1805, https://doi.org/10.1016/j.jcin.2017.06.020 (2017).
33. Otsuka, F. *et al*. Pathology of Second-Generation Everolimus-Eluting Stents Versus First-Generation Sirolimus- and Paclitaxel-Eluting Stents in Humans. *Circulation* **129**, 211–223, https://doi.org/10.1161/Circulationaha.113.001790 (2014).
34. Gori, T. *et al*. Predictors of stent thrombosis and their implications for clinical practice. *Nat. Rev. Cardiol.* **16**, 243–256, https://doi.org/10.1038/s41569-018-0118-5 (2019).
35. Finn, A. V. *et al*. Differential response of delayed healing and persistent inflammation at sites of overlapping sirolimus- or paclitaxel-eluting stents. *Circulation* **112**, 270–278, https://doi.org/10.1161/Circulationaha.104.508937 (2005).
36. Raber, L. *et al*. Impact of Stent Overlap on Angiographic and Long-Term Clinical Outcome in Patients Undergoing Drug-Eluting Stent Implantation. *J. Am. Coll. Cardiology* **55**, 1178–1188, https://doi.org/10.1016/j.jacc.2009.11.052 (2010).
37. Schwartz, R. S. *et al*. Restenosis and the Proportional Neointimal Response to Coronary-Artery Injury - Results in a Porcine Model. *J. Am. Coll. Cardiology* **19**, 267–274, https://doi.org/10.1016/0735-1097(92)90476-4 (1992).
38. Nakano, M. *et al*. Human autopsy study of drug-eluting stents restenosis: histomorphological predictors and neointimal characteristics. *Eur. Heart J.* **34**, 3304–+, https://doi.org/10.1093/eurheartj/eht241 (2013).
39. Dweck, M. R. *et al*. Coronary arterial 18F-sodium fluoride uptake: a novel marker of plaque biology. *J. Am. Coll. Cardiol.* **59**, 1539–1548, https://doi.org/10.1016/j.jacc.2011.12.037 (2012).
40. Hutcheson, J. D., Maldonado, N. & Aikawa, E. Small entities with large impact: microcalcifications and atherosclerotic plaque vulnerability. *Curr. Opin. Lipidol.* **25**, 327–332, https://doi.org/10.1097/MOL.0000000000000105 (2014).
41. Dweck, M. R. *et al*. Noninvasive Molecular Imaging of Disease Activity in Atherosclerosis. *Circ. Res.* **119**, 330–340, https://doi.org/10.1161/CIRCRESAHA.116.307971 (2016).
42. Tearney, G. J. *et al*. Quantification of macrophage content in atherosclerotic plaques by optical coherence tomography. *Circulation* **107**, 113–119, https://doi.org/10.1161/01.cir.0000044384.41037.43 (2003).
43. Phipps, J. E. *et al*. Macrophages and intravascular OCT bright spots: a quantitative study. *JACC Cardiovasc. Imaging* **8**, 63–72, https://doi.org/10.1016/j.jcmg.2014.07.027 (2015).
44. Chu, K. K. *et al*. *In vivo* imaging of airway cilia and mucus clearance with micro-optical coherence tomography. *Biomed. Opt. Express* **7**, 2494–2505, https://doi.org/10.1364/BOE.7.002494 (2016).
45. Cui, D. *et al*. Flexible, high-resolution micro-optical coherence tomography endobronchial probe toward *in vivo* imaging of cilia. *Opt. Lett.* **42**, 867–870, https://doi.org/10.1364/OL.42.000867 (2017).
46. Yin, B. W., Hyun, C., Gardecki, J. A. & Tearney, G. J. Extended depth of focus for coherence-based cellular imaging. *Optica* **4**, 959–965, https://doi.org/10.1364/Optica.4.000959 (2017).
47. Yin, B. W. *et al*. 3D cellular-resolution imaging in arteries using few-mode interferometry. *Light-Sci Appl* **8**, https://doi.org/10.1038/s41377-019-0211-5 (2019).
48. Schwartz, R. S., Chronos, N. A. & Virmani, R. Preclinical restenosis models and drug-eluting stents: still important, still much to learn. *J. Am. Coll. Cardiol.* **44**, 1373–1385, https://doi.org/10.1016/j.jacc.2004.04.060 (2004).
49. Kim, S. *et al*. Intracoronary dual-modal optical coherence tomography-near-infrared fluorescence structural-molecular imaging with a clinical dose of indocyanine green for the assessment of high-risk plaques and stent-associated inflammation in a beating coronary artery. *Eur. Heart J.* **37**, 2833–2844, https://doi.org/10.1093/eurheartj/ehv726 (2016).
50. Schurgers, L. J. *et al*. Vitamin K-Antagonists Accelerate Atherosclerotic Calcification and Induce a Vulnerable Plaque Phenotype. *Plos One* 7, https://doi.org/10.1371/journal.pone.0043229 (2012).

Acknowledgements

We thank Yeon Hoon Kim for advice on operating conventional OCT system. This research was supported by grants through the National Research Foundation of Korea (NRF) funded by the Ministry of Education, Science and Technology (grant numbers: NRF-2015R1A1A1A05027209, NRF-2019M3A9E2066880, NRF-2018R1A2B3002001 and NRF-2019M3A9E2066882), and the Establish R&D Platform Project through the Korea University Medical Center and Korea University Guro Hospital, funded by the Korea University Guro Hospital (grant number: O1903851).

Author contributions

J.K. and M.W.L., developed the imaging system; J.K., S.K., J.W.S., J.H. and H.J.K. performed imaging studies and acquired the data; J.K., S.K. and J.W.S. analyzed the data; J.K., S.K. and J.W.S. drafted the manuscript; J.W.K. and H.Y. handled funding and supervision. J.W.K. and H.Y. conceived the original idea, designed the research and revised whole manuscript. All authors discussed the results and commented on the manuscript.

Competing interests

The authors declare no competing interests.

Additional information

Supplementary information is available for this paper at https://doi.org/10.1038/s41598-020-65742-2.

Correspondence and requests for materials should be addressed to J.W.K. or H.Y.

Reprints and permissions information is available at www.nature.com/reprints.